

Active Learning of Uniformly Accurate Inter-atomic Potentials for Materials Simulation

Linfeng Zhang

*Program in Applied and Computational Mathematics,
Princeton University, Princeton, NJ 08544, USA*

De-Ye Lin

*Institute of Applied Physics and Computational Mathematics,
Huayuan Road 6, Beijing 100088, P.R. China and
CAEP Software Center for High Performance Numerical Simulation, Huayuan Road 6, Beijing 100088, P.R. China*

Han Wang*

*Laboratory of Computational Physics, Institute of Applied Physics and
Computational Mathematics, Huayuan Road 6, Beijing 100088, P.R. China*

Roberto Car

*Department of Chemistry, Department of Physics,
Program in Applied and Computational Mathematics,
Princeton Institute for the Science and Technology of Materials,
Princeton University, Princeton, NJ 08544, USA*

Weinan E[†]

*Department of Mathematics and Program in Applied and Computational Mathematics,
Princeton University, Princeton, NJ 08544, USA and
Beijing Institute of Big Data Research, Beijing, 100871, P.R. China*

An active learning procedure called Deep Potential Generator (DP-GEN) is proposed for the construction of accurate and transferable machine learning-based models of the potential energy surface (PES) for the molecular modeling of materials. This procedure consists of three main components: exploration, labeling, and training. Application to the sample systems of Al, Mg and Al-Mg alloys demonstrates that DP-GEN can generate uniformly accurate PES models with a minimum number of labeled data.

Keywords:

INTRODUCTION

The inter-atomic potential energy surface (PES) plays a central role in the molecular modeling of materials. Obtaining an accurate and efficient representation of the PES is a central issue in molecular simulation. In this context, one faces the dilemma that *ab initio* methods are accurate but highly inefficient, while empirical force fields (FFs) are efficient, but there is a limited guarantee for their accuracy. Thus, there is a great demand for an efficient and uniformly accurate PES model that can be used to compute a broad range of atomistic properties for most material compounds of practical interest.

Developing empirical FFs has been challenging due to the high dimensionality and many-body character of the PES. Usually, empirical FFs parameterize the PES by assuming an analytical functional form in terms of relatively simple functions based on physical/chemical intuitions and by fitting the model parameters against a bundle of experimental properties and/or microscopic quantities from *ab initio* calculations. Some popular examples are the Lennard-Jones potential [1], the Stillinger-Weber

potential [2], the embedded-atom method (EAM) potential [3], the CHARMM [4]/AMBER [5] FFs, the reactive FFs [6], etc. *Representability* and *transferability* are two main issues faced by empirical FFs. By representability, we mean the ability of the assumed functional form to reproduce accurately the target properties. By transferability, we mean the ability of a PES model to describe properties that do not belong to the set of fitting targets. Due to the physical/chemical knowledge encoded in the functional form, we expect the empirical FFs to be qualitatively transferable to a moderate range of thermodynamic conditions beyond those adopted for the fitting. However, as a consequence of assuming relatively simple functional forms, empirical FFs usually face a severe representability problem. Moreover, a substantial human effort in tuning the model parameters is often required to achieve the best balance in fitting the target properties.

Recent progress with machine learning (ML) methods is changing the outlook in this context [7–19]. ML models, being capable of learning complex and highly non-linear functional dependence, are excellent in their representability. It is now possible, using modern ML ap-

proaches, to parametrize the PES using data from *ab initio* calculations to obtain models that have *ab initio* accuracy and are, at the same time, competitive regarding efficiency against empirical FFs. Despite the remarkable success of these ML methods, their transferability is often in doubt, i.e. the ML models are usually believed to be poor in predicting the properties of a configuration that is far from the training dataset. In addition, since labeling is usually done with expensive first-principle calculations, one would like to obtain reliable ML models without having to rely on too large labeled datasets. These questions arise not just for PES modeling, but in many other contexts when ML methods are applied to problems involving physical models.

To address this issue, we get inspiration from active learning [20, 21], an area of supervised learning whose aim is to learn general purpose models with a minimal number of labels. In the context of active learning, one typically faces a situation in which unlabeled data are abundant, but labeling is expensive. Therefore, an interactive algorithm is required to efficiently explore unlabeled data, collect feedbacks on-the-fly, and actively query the teacher for labels on data points with negative feedbacks. Along this line of thinking, at an abstract level, one can formulate an active learning procedure for PES modeling that involves three s-eps-converted-to.pdf: exploration, labeling, and training.

1. *Exploration* requires an efficient *sampler* and an informative *indicator*. The sampler uses the current PES model to quickly explore the configuration space. The indicator monitors on-the-fly the configurations explored by the sampler, selects those with low prediction accuracy, and sends them to the labeling step.
2. *Labeling* means mapping the selected configurations to accurate labels, i.e., energies and forces. Labeling can be done by a code that implements high-level quantum chemistry, quantum Monte Carlo, or density functional theory (DFT) methods. The labeled configurations are then *added* to the existing dataset and used in the new iteration for training.
3. *Training* requires a good *model*, or PES representation, which can fit the ever-increasing dataset with satisfactory accuracy. Such a representation should be efficient and should satisfy certain physical constraints like the extensive and symmetry-preserving properties of the PES.

The whole scheme falls into a closed loop: One starts with a relatively poor approximation of the PES and uses it to explore different configurations. Then a selected set of new configurations is labeled, and a new approximation of the PES is obtained by training. These three

s-eps-converted-to.pdf are repeated until convergence is achieved, i.e., the configuration space has been explored sufficiently, and a minimal set of data points have been accurately labeled. At the end of this procedure, a uniformly accurate PES model is generated.

In this work, our first goal is to translate the general proposal described above into a practical scheme for modeling the PES of materials. We expect that this scheme should allow us to generate uniformly accurate PES models for different material compounds systematically and, to a large extent, automatically. In this scheme, we use an advanced version of the Deep Potential (DP) model [19], which has shown great promise in learning the PES of a broad range of systems, including a 5-component high entropy alloy. For the sampler, we use molecular dynamics (MD) based on the DP model. Thereafter DP based MD will be referred to as DPMD. At the same time, we introduce an indicator that we call the model deviation. This is done as follows. We train an ensemble of DP models using the same dataset but different initialization of the parameters. For each new configuration that is explored by DPMD, these models generate an ensemble of predictions. For each such configuration, the model deviation is defined as the maximum standard deviation of the predicted atomic forces. A high model deviation indicates a low quality in the model prediction and should be proposed for labeling. In this work, we use in the labeling stage DFT within the generalized gradient approximation [22–25], which works well in the chosen testing examples. We will see that sampling is much cheaper than labeling, and only a very small fraction of the explored configurations is selected for labeling. We call the methodology introduced here the Deep Potential Generator, abbreviated DP-GEN.

Our second goal is to demonstrate the uniform accuracy of the PES model obtained this way. To this end, we consider the example of Al, Mg, as well as Al-Mg alloys. Using DP-GEN, we construct a model that can accurately describe these systems at different compositions and thermodynamic conditions. The resulting PES model is evaluated from the point of view of a material scientist. We calculate several static, dynamical, thermal, and mechanical properties, such as phonon spectra, radial distribution functions (RDF), elastic constants, etc. Some of these properties are compared with DFT results. We compare DP calculated properties directly with experimental results when these are available. To further test the quality of the PES model, we introduce an automatic procedure based on the Materials Project (MP) database [26]. In this procedure, one searches the database by entering a material composition, such as Al-Mg in the present case. The database will then return a large number of locally stable structures, including many structures of potential practical interest. Based on these structures, we evaluate several equilibrium properties and compare the DFT predictions with those of the

PES model. In addition, for each one of these structures, we automatically generate unrelaxed vacancy and interstitial defects as well as the set of surfaces corresponding to a range of Miller indices [27]. We then compare the relaxed formation energies of the defects and the unrelaxed formation energies of the surfaces predicted by DFT and by the PES model. We stress that these structures, i.e., crystals, defects, and surfaces, were not explicitly included in the training data. We find that our PES model can achieve uniform accuracy in the prediction of all of these structural properties.

We stress that there is a difference between active learning in conventional ML problems and the active learning we pursue here. This difference lies in exploration or sampling. Conventional active learning problems in ML typically deal with an existing unlabeled dataset. Here our dataset is generated on the fly via sampling. This means that we need to have an efficient sampling method.

We should mention that related work can be found in the literature [28–31]. In particular, Smith et al [29] utilized an active learning scheme to model the PES of organic molecules based on an existing large database [32]. In addition, Bartok et al [33] constructed a kernel based general purpose PES model for pure silicon, wherein for labeling they exhaustively enumerated possible structures. Finally, the principle of active learning was also used in the reinforced dynamics scheme [34] for enhanced sampling and free energy calculation. The present work is the first in which starting from little *a priori* knowledge, configuration exploration, labeling, and training are all combined to form a closed loop. This is a general procedure that is of interest for the application of ML to different physical modeling problems, like, e.g., in fluid dynamics [35].

METHODOLOGY

In this section, we introduce the three essential components of the DP-GEN scheme: the model, the sampler, and the indicator. Fig. 1 shows a schematics of DP-GEN. To initialize the procedure, we label a small set of initial structures introduced in Fig. 1(a) and train an ensemble of preliminary DP models. More details on the simulation protocol and the iterative process are reported in the supplementary materials (SM).

Model. The DP scheme assumes that the potential energy E can be written as a sum of atomic energies, i.e., $E = \sum_i E^i$. Each atomic energy E^i is a function of \mathcal{R}^i , the local environment of atom i in terms of the relative coordinates of its neighbors within a cut-off radius r_c . The dependence of E^i on \mathcal{R}^i embodies the nonlinear and many-body character of the inter-atomic interactions. Therefore, we use a deep neural network function (DNN) to parameterize it, i.e., $E^i = E^{w_{\alpha_i}}(\mathcal{R}^i)$. Here

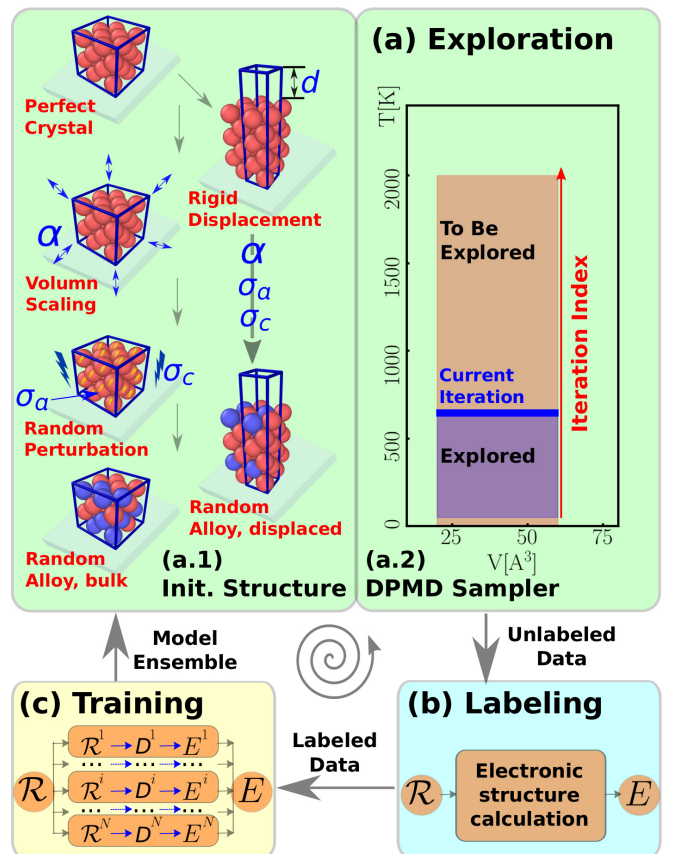


FIG. 1: Schematic plot of one iteration of the DP-GEN scheme, taking the Al-Mg system as an example. (a) Exploration with DPMD. (a.1) Preparation of initial structures. I. For bulk structures: start from stable crystalline structures of pure Al and Mg. In this work, we only use face-centered-cubic (FCC), hexagonal-closed-packed (HCP), simple cubic (SC), and diamond structures. II. Compress and dilate the stable structures uniformly to allow for a larger range of number densities. We use α to denote the scale factor of the compression and dilation operations. Here α ranges in the interval 0.96-1.04. III. Randomly perturb the atomic positions and cell vectors of all the initial crystalline structures. The magnitude of perturbations on the atomic coordinates is $\sigma_a = 0.01\text{\AA}$. The magnitude of perturbation on each cell vector is $\sigma_c = 0.03$ times the length of the cell vector. IV. Generate random alloy structures: starting from all the structures prepared for pure systems, randomly place Al or Mg at different sites. V. Generate structures with rigid displacement: starting from stable FCC and HCP structures, rigidly displace two crystalline halves along specific crystallographic directions. We only use (100), (110), (111), and (0001), (10 $\bar{1}$ 0), (11 $\bar{2}$ 0), respectively, for FCC and HCP, as the displacement directions. The magnitudes d of the displacements range in the interval 0.2-10.0 \AA . Based on all the displaced structures, perform dilation α and perturbation σ_a and σ_c , and generate random alloy structures. (a.2) Canonical simulation at a given temperature. The temperature increases with the iteration index within the range 50-2000 K. (b) Labeling with electronic structure calculations. (c) Training with the DP model.

α_i indicates the chemical species of the i -th atom; \mathbf{w}_{α_i} denotes the parameters of the DNN to be determined by the training procedure. A vital component of the DP model is a general procedure that encodes \mathcal{R}^i into the so-called feature matrix \mathcal{D}^i . This procedure guarantees the conservation of the translational, rotational, and permutational symmetries of the system, without losing coordinate information in the local environment. Derivatives of the energy with respect to the atomic positions give the forces. During the training process, the parameters of the DP model evolve in order to minimize the loss function, a measure of the error in the energies and the forces predicted by DP relative to the labels, i.e., the corresponding DFT predictions [36]. Upon convergence, the model can match the labels within a small error tolerance. The details of the architecture of the DP model and the training process are given in Ref. [19].

Sampler. The goal of the sampler is to explore the configuration space in a range of thermodynamic variables, say temperature and pressure. Ideally one should develop an automatic/adaptive procedure for this purpose. However, since exploration is relatively cheap compared with labeling, we adopt a more heuristic approach in which the exploration is done through: (1) carefully selecting the initial configurations, and (2) exploring the volume-temperature space. We use a variety of crystal structures as our initial configuration, as in the procedure illustrated in Fig. 1(a). To explore the volume-temperature phase space, we adopt a temperature increasing scheme, in which the temperature of the DPMD simulations is increased systematically with the iteration index in the range 50-2000 K. We notice that many structures constructed in this way are far from equilibrium structures so that the subsequent DPMD simulation in the 50-2000K temperature range produces a large sample of configurations that may differ substantially from the initial structure. More details on the initial structures and the thermodynamic conditions in each iteration are summarized in Tables S1–S4.

Indicator. It is well-known that neural network models are highly nonlinear functions of the parameters, and different initializations of the parameters often lead to different minimizers of the loss function. These minimizers generate equally accurate energies and forces in the configurational region belonging to the neighborhood of the training data, but they usually show significantly larger deviation for snapshots “far” from the training data. This property of neural network models motivates us to define the indicator as the deviation of the predictions generated by an ensemble of DP models trained with the same dataset but with different parameter initializations. In practice, we define the model deviation, denoted as \mathcal{E} , as the maximum standard deviation of the

predictions for the atomic forces, i.e.:

$$\mathcal{E} = \max_i \sqrt{\langle \|\mathbf{f}_i - \bar{\mathbf{f}}_i\|^2 \rangle}, \quad \bar{\mathbf{f}}_i = \langle \mathbf{f}_i \rangle, \quad (1)$$

where i runs through the atomic indices in a configuration, and the ensemble average $\langle \dots \rangle$ is taken over the ensemble of models. We find that using the force predictions to evaluate the model deviation is generally better than using the energy predictions. The force is an atomic property and is sensitive to a failure in local predictions, while the energy is a global quantity and does not seem to provide sufficient resolution in this regard. Moreover, we find that the failure in local predictions can be better signaled by using the maximum over i in Eqn. 1, instead of using an average over i ($\frac{1}{N} \sum_i$).

RESULTS AND DISCUSSION

As examples, we report the results of the DP-GEN scheme for Al, Mg and their alloys. At the end of the DP-GEN scheme, we collect a set of labeled data and obtain a DP model for the Al-Mg system. As shown in Table S4, about 650 million configurations were explored by DPMD, but only 0.0044% of them were selected for labeling. To get an idea of the usefulness of the resulting DP model for materials science applications, we compare the accuracy of the DP model in predicting important material properties with a state-of-the-art empirical FF such as the modified embedded atom method (MEAM) [37]. MEAM adopts a more general definition of embedding than EAM in order to improve the description of directional bonding and of alloy systems. In this work, we compare our method with a very recent version of the Al-Mg MEAM potential that is available in the literature [38]. We used the DeePMD-kit package [39] in the training step, the LAMMPS package [40] in the exploration step, and the VASP package [23, 24] in the labeling step.

Pure Al and Mg

The equilibrium properties of pure Al are presented in Table I, including the atomization energy and equilibrium volume per atom, defect formation energies, elastic constants and moduli, stacking fault energies, melting point, enthalpy of fusion, and diffusion coefficient. The defect formation energy is defined as $E_{\text{df}} = E_{\text{d}}(N_{\text{d}}) - N_{\text{d}}E_0$, $d = v(i)$ indicating vacancy (interstitial) defects. E_{d} denotes the relaxed energy of a defective structure with N_{d} atoms and E_0 denotes the energy per atom of the corresponding ideal crystal at $T = 0$ K. To compute the defect formation energies, we use a supercell in which we replicate $7 \times 7 \times 7$ times the primitive FCC cell.

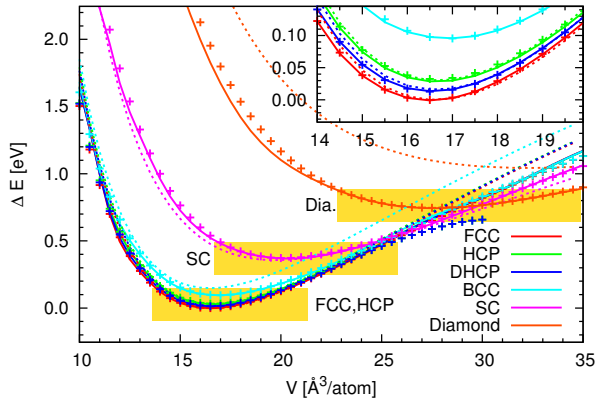


FIG. 2: The EOS's of Al. Solid lines, dashed lines, and cross points denote DP, MEAM, and DFT results, respectively. The energies of MEAM are shifted so that the MEAM energy of a stable FCC structure equals to that given by DFT. DFT based relaxations fail in some HCP and DHCP structures with a volume per atom larger 30 \AA^3 , thus the corresponding DFT predictions are not shown. Yellow bars denote volume ranges in the training data. The BCC and DHCP structures are not explicitly added to the training data.

We estimate the melting temperature (T_m) by simulating with DPMD coexisting crystal and liquid phases in a supercell containing 8000 atoms within the isothermal-isobaric ensemble at standard pressure. To estimate the liquid diffusion coefficient (D), we perform DPMD simulations on large supercells (6912 atoms) for which finite size effects are negligible. For all the properties in Table I, the DP predictions are in satisfactory agreement with DFT and/or experiment. Notice that MEAM reproduces quite accurately the solid state properties in Table I, particularly when compared to experiment, which is not surprising since the basic experimental solid state properties have been used to tune the parameters of the FF. However, the vibrational properties at short wavelength, particularly the zone boundary phonons, are not reproduced well by MEAM in contrast to DP, as shown in Fig. 3. MEAM fails even more dramatically in predicting the properties of the liquid: the MEAM liquid is largely overstructured (see Fig. 4). Its diffusion coefficient is one order of magnitude smaller than in experiment or DP, and its enthalpy of fusion is also significantly smaller than in experiment or DP (see Table I).

DFT, DP and MEAM predictions for the equation of state (EOS) of Al are reported in Fig. 2. DP reproduces well the DFT results for all the crystalline structures considered here, i.e., FCC, HCP, double-hexagonal-closed-packed (DHCP), body-centered-cubic (BCC), SC and diamond. Interestingly, the range of DP accuracy extends well beyond the volume interval that was included in the training data, which is indicated by the yellow shaded area in the figure. As shown in the inset of Fig. 2, the

TABLE I: Equilibrium properties of Al: atomization energy E_{am} , equilibrium volume per atom V_0 , vacancy formation energy E_{vf} , interstitial formation energies E_{if} for octahedral interstitial (oh) and tetrahedral interstitial (th), independent elastic constants C_{11} , C_{12} , and C_{44} , Bulk modulus B_V (Voigt), shear modulus G_V (Voigt), stacking fault energy γ_{sf} , twin stacking fault energy γ_{tsf} , melting point T_m , enthalpy of fusion ΔH_f , and diffusion coefficient D at $T = 1000\text{K}$.

Al	EXP	DFT ^a	DP	MEAM
E_{am} [eV/atom]	-3.49 ^b	-3.655	-3.654	-3.353
V_0 [$\text{\AA}^3/\text{atom}$] ^c	16.50 ^d	16.48	16.51	16.61
E_{vf} [eV]	0.66 ^e	0.67 ^f	0.79	0.67
E_{if} (oh) [eV]	-	2.91 ^f	2.45	2.77
E_{if} (th) [eV]	-	3.23 ^f	3.12	3.32
C_{11} [GPa]	114.3 ^g	111.2	120.9	111.4
C_{12} [GPa]	61.9 ^g	61.4	59.6	61.4
C_{44} [GPa]	31.6 ^g	36.8	40.4	29.7
B_V [GPa]	79.4 ^g	78.0	80.1	78.1
G_V [GPa]	29.4 ^g	32.1	36.5	27.0
γ_{sf} [J/m^2]	0.11–0.21 ^h	0.142 ⁱ	0.132	0.143
γ_{tsf} [J/m^2]	-	0.135 ⁱ	0.130	0.144
T_m [K]	935 ^j	950(± 50) ^k	918(± 5)	898(± 5)
ΔH_f [kJ/mol]	10.7(± 0.2) ^l	-	10.2	4.4
D [$10^{-9}\text{m}^2/\text{s}$]	7.2–7.9 ^m	-	7.1	0.4

^aThe DFT results, unless specified with a reference, are computed by the authors. We notice that a K-mesh spacing equal to 0.06 \AA^{-1} was used to obtain more converged DFT results in this table. However, in the labeling stage, we used a K-mesh spacing equal to 0.08 \AA^{-1} , which gives converged values for most of the properties except for elastic constants and moduli. Using K-mesh spacing equal to 0.08 \AA^{-1} gives $C_{11} = 129.3 \text{ GPa}$, $C_{12} = 52.8 \text{ GPa}$, $C_{44} = 37.4 \text{ GPa}$, $B_V = 78.3 \text{ GPa}$, and $G_V = 37.7 \text{ GPa}$. ^bRef. [41]. ^cExperiment values obtained at $T = 298\text{K}$; DFT, DP, and MEAM results obtained at $T = 0\text{K}$. ^dRef. [42]. ^eRefs. [43, 44]. ^fRef. [45]. ^gRef. [46]. ^hRefs. [47–50]. ⁱRef. [51]. ^jRef. [52]. ^kRef. [53]. ^lRef. [54]. ^mRef. [55], $D = 7.2 \times 10^{-9}\text{m}^2/\text{s}$ at 980K and $7.9 \times 10^{-9}\text{m}^2/\text{s}$ at 1020K .

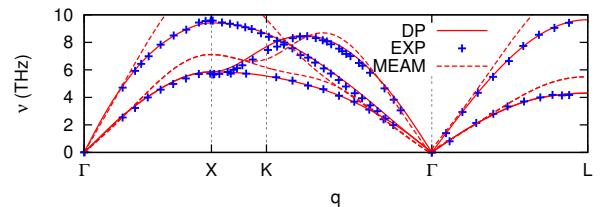


FIG. 3: The phonon dispersion relations of Al at $T = 80\text{K}$ and $P = 1\text{bar}$. The experimental data is taken from [56].

energy difference between FCC and DHCP, and the one between DHCP and HCP is small, only 12 meV/atom and 19 meV/atom, respectively, yet DP reproduces accurately the relative stabilities. The MEAM potential performs well for FCC, HCP, DHCP, and SC, but shows significant deviations from DFT for diamond and BCC. DP and MEAM predictions for the phonon dispersion relations are compared with experimental results in Fig. 3. DP results agree very well with experiment.

The promise of ML potential models is to retain the

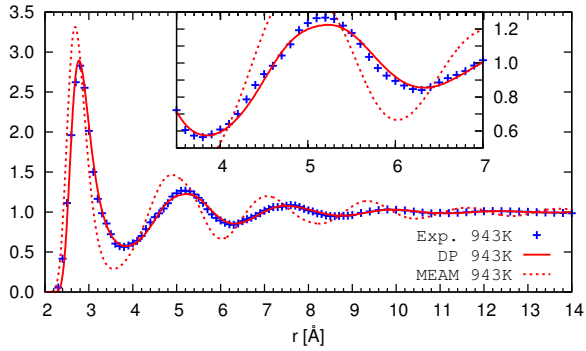


FIG. 4: The RDFs of liquid Al at $P = 1$ bar and temperatures $T = 943$ K. The DP and MEAM predictions are compared with the experimental data taken from [57]. The inserted plot is the zoom-in of RDFs in range $3.5\text{\AA} \leq r \leq 7\text{\AA}$.

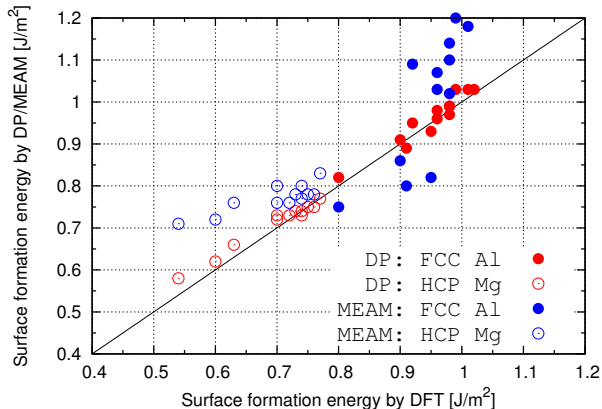


FIG. 5: Surface formation energies of Al and Mg. All the non-equivalent surfaces with Miller index values smaller than 4 and 3 are investigated for Al and Mg, respectively.

accuracy of *ab initio* molecular dynamics (AIMD) at the cost of FF simulations. Therefore, ML potential models can be used to simulate much larger systems for much longer times than possible with AIMD. This is illustrated by our calculations of the diffusion coefficient and of the radial distribution function (RDF) of the liquid, which were performed on large cells with 4000 atoms with very modest computational resources when using DP. Thus, the DP model opens up great opportunities for extending the power of *ab initio* methods.

The DP method gives similarly good results for the corresponding properties of pure Mg, which are reported in the SM.

Finally, we examine the surface formation energy $E_{\text{sf}}((lmn))$, which describes the energy needed to create a surface with Miller indices (lmn) for a given crystal, and is defined by $E_{\text{sf}}((lmn)) = \frac{1}{2A}(E_s((lmn)) - N_s E_0)$. Here $E_s((lmn))$ and N_s denote the energy and number of atoms of the relaxed surface structure with Miller indices (lmn) . A denotes the surface area. We enumerate

all the non-equivalent surfaces corresponding to Miller index values smaller than 4 for Al, and smaller than 3 for Mg. As shown in Fig. 5, the surfaces formation energies predicted by DP are close to DFT [58], and those predicted by MEAM are worse in all cases. We report in detail the values of surface formation energies for Al and Mg in Tables S6 and S7, respectively.

Mg-Al Alloys

For alloy systems, we adopted the testing scheme introduced in Section I, finding 28 crystalline (ordered) Mg-Al alloy structures in the MP database [26], corresponding to relative Mg concentrations (c_{Mg}) ranging from 25% to 94%. Most of these structures were found initially from experiment and were recorded in the inorganic crystal structure database (ICSD) [59]. When recorded in the MP database they were further relaxed with DFT. In Figs. 6 (a-f), we compare predictions of DFT, DP, and MEAM for the 28 alloy structures. The 6 panels in Fig. 6 report (a) the formation energies, (b) the equilibrium volumes per atom, (c) the elastic constants, (d) the relaxed vacancy formation energies, (e) the total energies per atom along interstitial relaxation pathways, and (f) the unrelaxed surface formation energies. Notice that only the elastic constants from DP are compared with DFT in Fig. 6 (c). The corresponding MEAM elastic constants are compared with DFT in Fig. S3.

The formation energy of an Mg-Al alloy system is defined as

$$E_{\text{af}} = E_0(c_{\text{Mg}}) - c_{\text{Mg}}E_{\text{Mg}}^0 - (1 - c_{\text{Mg}})E_{\text{Al}}^0$$

where $E_0(c_{\text{Mg}})$ denotes the equilibrium energy (0 K) per atom of the Mg-Al alloy structure with Mg concentration equal to c_{Mg} , and E_{Mg}^0 and E_{Al}^0 denote the equilibrium energies per atom of the corresponding stable crystals of pure Mg and Al at 0 K. The precise values of the formation energies and equilibrium volumes per atom are reported in Table S9. To generate the vacancy and interstitial structures, we used supercells that are periodic copies of the MP structures. The size of the supercell for each MP structure is reported in Table S5. We further notice that the interstitial structures are automatically generated based on 12 MP structures [68] that are the most stable ones at the corresponding concentrations. Since most of the interstitial structures are energetically highly unstable, their relaxation will likely end up with structures that do not represent locally relaxed interstitial point defects, as shown in Fig. S4. In this case, the end structures depend very sensitively on the details of the relaxation. Therefore, instead of performing independent relaxation within DFT, DP, and MEAM, we compare the predictions of these methods for configurations along the DFT relaxation pathways (excluding the initial high energy configuration).

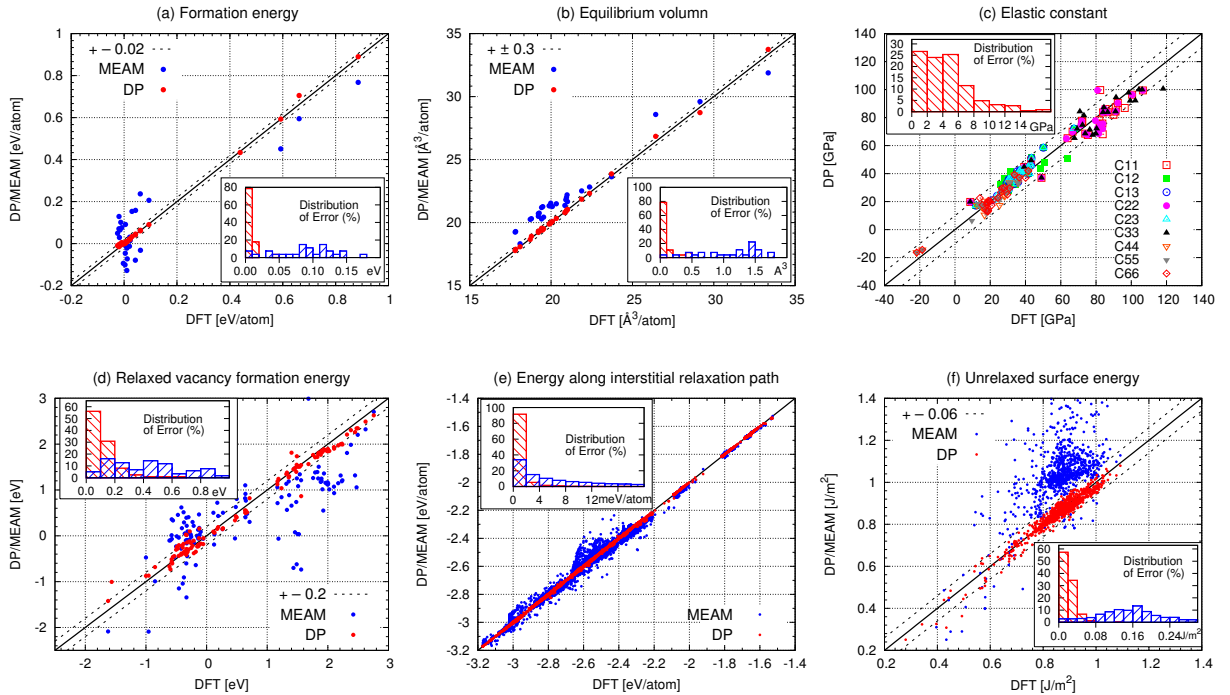


FIG. 6: Comparisons of Al-Mg alloy properties predicted by DFT, DP, and MEAM, based on 28 structures in the MP database. (a) 28 formation energies. (b) 28 equilibrium volumes per atom. (c) 225 elastic constants. Three structures, mp-1039192, mp-1094664, and mp-12766, are excluded because they resulted unstable under small displacements within DFT. (d) 125 relaxed vacancy formation energies. Three structures, mp-1039192, mp-1094664, and mp-1038818, are excluded because they resulted unstable under vacancy relaxations within DFT. Two DP predictions and three MEAM predictions are outside the range of the plot due to large errors. (e) 86,199 energies per atom along the interstitial relaxation pathways within DFT. (f) 903 unrelaxed surface energies.

In almost all tested cases, we observe an overall satisfactory agreement between DP predictions and DFT reference results. The accuracy of DP is significantly better than that of MEAM. We stress that the DP-GEN procedure is blind to the alloy structures used to compute the properties reported in Fig. 6, because these structures were not explicitly included in the training data. The number of atoms in the unit cell of 6 MP structures is larger than 32, which is the maximum number of atoms in the unit cell of the structures belonging to the training dataset. This suggests that in the case of Mg-Al alloys the DP model trained with relatively small periodic structures can, to some extent, be used to predict the properties of larger structures. Some structures tested have little in common with the initial training data. Yet the DP model gave satisfactory results, giving us confidence that it should work in a broad range of materials science problems.

SUMMARY

The DP-GEN scheme is general, practical, and fairly automatic. To generate the DP model for the Al-Mg sys-

tem, we did not use any existing DFT database (the MP database was only used for testing), nor did we use an exhaustive list of possible structures based on physical and chemical considerations. Instead, we explored the space of configurations using computationally efficient DPMD simulations. DFT calculations were only performed on a small subset of the configurations that showed large model deviation. This made possible to progressively improve the DP model. We expect that this strategy should also work for a large variety of other systems and that it should provide a uniformly accurate description of the PES for those systems.

The DP-GEN scheme is also quite flexible. The three components, training, exploration, and labeling, are highly modularized and can be implemented separately and then recombined. This makes it easy to incorporate additional functionalities. For example, enhanced sampling techniques [31] or genetic algorithms [60] can be incorporated with minimal effort in the exploration module. We expect that the modular structure of DP-GEN will make possible to use this method to generate models for a variety of important problems, such as finding transition pathways for structural transformations and chemical reactions.

The work of L.Z. and W.E is supported in part by Major Program of NNSFC under grant 91130005, ONR grant N00014-13-1-0338 and NSFC grant U1430237. The work of L.Z. and R.C. is supported in part by the DOE with Award Number DE-SC0019394. The work of H.W. is supported by the National Science Foundation of China under Grants 11501039, 11871110 and 91530322, and the National Key Research and Development Program of China under Grants 2016YFB0201200 and 2016YFB0201203. The work of D.Y.L. and H.W. is supported by the Science Challenge Project No. JCKY2016212A502. We are grateful for computing time provided in part by the National Energy Research Scientific Computing Center (NERSC), the Terascale Infrastructure for Groundbreaking Research in Science and Engineering (TIGRESS) High Performance Computing Center and Visualization Laboratory at Princeton University, the Special Program for Applied Research on Super Computation of the NSFC-Guangdong Joint Fund under Grant No. U1501501, and the Beijing Institute of Big Data Research.

SUPPLEMENTARY MATERIAL

Simulation protocol

Model The smooth edition of the deep potential [19] model is adopted in this work. The cut-off radius is set to 9 Å. The $1/r$ terms in the network construction is smoothly switched-off by a cosine shape function [19] from 2 Å to 9 Å so that the discontinuity due to the cut-off is removed. The filter (embedding) net is of size {25, 50, 100}, and the fitting net is of size {240, 240, 240}. A skip connection is built between two neighboring layers, so the architecture of the network is ResNet-like [61]. The Adam stochastic gradient descent method [36] is adopted to train the models, with a learning rate starting at 5.0×10^{-4} and exponentially decaying to 1.8×10^{-8} in 400,000 training s-eps-converted-to.pdf. Four models with the same data and training setting, but different parameter initializations, are trained to estimate the model deviation in the force prediction. After all the data are collected, the final model is trained with 1,280,000 training s-eps-converted-to.pdf.

Exploration Table S1, S2, and Table S3 report the exploration strategy in each iteration for pure Al, pure Mg, and Al-Mg alloy systems, respectively. During the exploration, if the model deviation of a configuration falls in the range [0.05, 0.15] eV/Å in the case of pure Al and Al-Mg alloy, or in range [0.03, 0.13] eV/Å in the case of pure Mg, then the corresponding configuration is selected for labeling. The number of atoms in each crystalline structure, the total number of explored and labeled configurations of each crystal structure are reported by Table S4.

Labeling The DFT simulation is carried out by the Vienna ab initio simulation package (VASP) version 5.4.4 [23, 24], within the Perdew-Burke-Ernzerhof generalized gradient approximation. The kinetic energy cutoff for the plane wave expansion is set to 600 eV, and the K-points is set with the Monkhorst-Pack mesh [25] at the spacing $h_k = 0.08 \text{ \AA}^{-1}$. The order 1 Methfessel-Paxton smearing method with $\sigma = 0.25 \text{ eV}$ is adopted. The self-consistent field (SCF) iteration will stop when the total energy and band structure energy differences between two consecutive s-eps-converted-to.pdf are smaller than 10^{-6} eV .

Additional simulation results

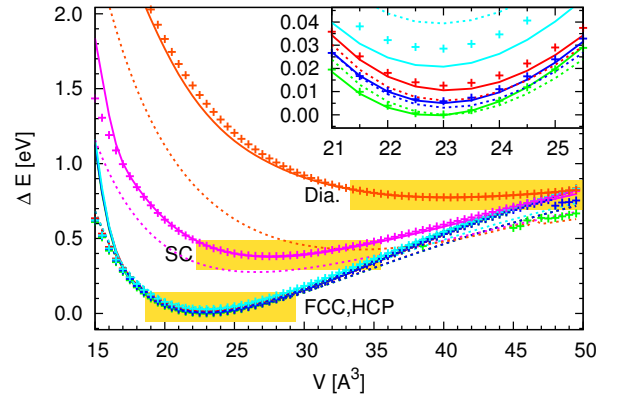


FIG. S1: Equation of states of Mg. Solid lines denotes DP results. Dashed lines denote MEAM results. Cross points denote DFT results. The energies of DP and MEAM are shifted so that the MEAM energy of a stable FCC structure equals to that given by DFT. The DFT relaxations fail in some HCP and DHCP structures with atomic volume larger 44 \AA^3 , thus the EOSs of HCP and DHCP beyond 44 \AA^3 are not shown.

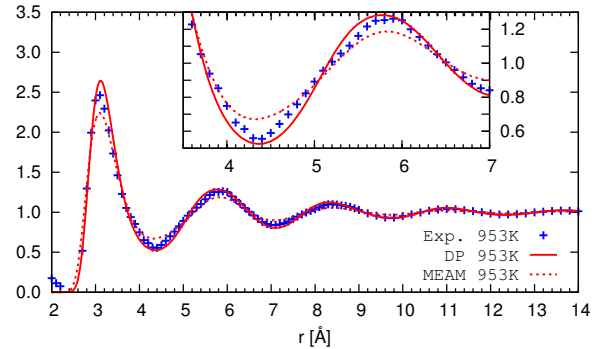


FIG. S2: The RDFs of liquid Mg at $P = 1 \text{ bar}$ and temperatures $T = 953 \text{ K}$. The DP and MEAM predictions are compared with the experimental data taken from [57]. The inserted plot is the zoom-in of RDFs in range $3.5 \text{ \AA} \leq r \leq 7 \text{ \AA}$.

TABLE S1: Exploration strategy for the pure Al system. For each iteration, we report the crystalline structure from which the initial structures are derived, the number of DPMD simulations, the length of DPMD trajectories, the statistical ensemble, the temperature of DPMD simulations and the portion of explored data sent to labeling. The pressure is 1 bar for the NPT ensembles.

Iter.	Crystal	#DPMD	Length [ps]	Ensemb.	T [K]	Labd. [%]	Iter.	Crystal	#DPMD	Length [ps]	Ensemb.	T [K]	Labd. [%]
0	FCC, HCP, DIA, SC	240	2	NVT	50	0.33	28	FCC, HCP	120	2	NVT	1500	0.10
1	FCC, HCP, DIA, SC	480	6	NVT	50	0.03	29	FCC, HCP	240	6	NVT	1500	0.06
2	FCC, HCP, DIA, SC	480	6	NVT	50	0.03	30	FCC, HCP	240	6	NVT	1500	0.06
3	FCC, HCP, DIA, SC	1200	6	NVT	50	0.01	31	FCC, HCP	600	6	NVT	1500	0.02
4	FCC, HCP, DIA, SC	240	2	NVT	100	0.08	32	FCC, HCP	120	2	NVT	2000	0.23
5	FCC, HCP, DIA, SC	480	6	NVT	100	0.02	33	FCC, HCP	240	6	NVT	2000	0.06
6	FCC, HCP, DIA, SC	480	6	NVT	100	0.03	34	FCC, HCP	240	6	NVT	2000	0.04
7	FCC, HCP, DIA, SC	1200	6	NVT	100	0.01	35	FCC, HCP	600	6	NVT	2000	0.02
8	FCC, HCP, DIA, SC	240	2	NVT	300	0.19	36	FCC(surf.)	792	0.2	NVT	300	0.69
9	FCC, HCP, DIA, SC	480	6	NVT	300	0.04	37	FCC(surf.)	792	2	NVT	300	0.08
10	FCC, HCP, DIA, SC	480	6	NVT	300	0.06	38	FCC(surf.)	792	6	NVT	300	0.03
11	FCC, HCP, DIA, SC	1200	6	NVT	300	0.01	39	FCC(surf.)	792	0.2	NVT	900	0.69
12	FCC, HCP	120	2	NVT	600	0.00	40	FCC(surf.)	792	2	NVT	900	0.08
13	FCC, HCP	240	6	NVT	600	0.05	41	FCC(surf.)	792	6	NVT	900	0.03
14	FCC, HCP	240	6	NVT	600	0.00	42	FCC(surf.)	792	0.2	NVT	1500	0.23
15	FCC, HCP	600	6	NVT	600	0.00	43	FCC(surf.)	792	2	NVT	1500	0.08
16	FCC, HCP	120	2	NVT	900	0.00	44	FCC(surf.)	792	6	NVT	1500	0.03
17	FCC, HCP	240	6	NVT	900	0.06	45	HCP(surf.)	792	0.2	NVT	300	0.00
18	FCC, HCP	240	6	NVT	900	0.06	46	HCP(surf.)	792	2	NVT	300	0.00
19	FCC, HCP	600	6	NVT	900	0.02	47	HCP(surf.)	792	6	NVT	300	0.00
20	FCC, HCP	120	2	NPT	900	0.00	48	HCP(surf.)	792	0.2	NVT	900	0.00
21	FCC, HCP	240	6	NPT	900	0.00	49	HCP(surf.)	792	2	NVT	900	0.03
22	FCC, HCP	240	6	NPT	900	0.00	50	HCP(surf.)	792	6	NVT	900	0.01
23	FCC, HCP	600	6	NPT	900	0.00	51	HCP(surf.)	792	0.2	NVT	1500	0.25
24	FCC, HCP	120	2	NVT	1200	0.12	52	HCP(surf.)	792	2	NVT	1500	0.07
25	FCC, HCP	240	6	NVT	1200	0.06	53	HCP(surf.)	792	6	NVT	1500	0.03
26	FCC, HCP	240	6	NVT	1200	0.06							
27	FCC, HCP	600	6	NVT	1200	0.02							

TABLE S2: Exploration strategy for the pure Mg system. For each iteration, we report the crystalline structure from which the initial structures are derived, the number of DPMD simulations, the length of DPMD trajectories, the statistical ensemble, the temperature of DPMD simulations and the portion of explored data sent to labeling. The pressure is 1 bar for the NPT ensembles.

Iter.	Crystal	#DPMD	Length [ps]	Ensemb.	T [K]	Labd. [%]	Iter.	Crystal	#DPMD	Length [ps]	Ensemb.	T [K]	Labd. [%]
0	FCC, HCP, DIA, SC	240	2	NVT	50	0.17	28	FCC, HCP	120	2	NVT	1500	0.00
1	FCC, HCP, DIA, SC	480	6	NVT	50	0.04	29	FCC, HCP	240	6	NVT	1500	0.04
2	FCC, HCP, DIA, SC	480	6	NVT	50	0.02	30	FCC, HCP	240	6	NVT	1500	0.03
3	FCC, HCP, DIA, SC	1200	6	NVT	50	0.01	31	FCC, HCP	600	6	NVT	1500	0.02
4	FCC, HCP, DIA, SC	240	2	NVT	100	0.21	32	FCC, HCP	120	2	NVT	2000	0.00
5	FCC, HCP, DIA, SC	480	6	NVT	100	0.01	33	FCC, HCP	240	6	NVT	2000	0.06
6	FCC, HCP, DIA, SC	480	6	NVT	100	0.01	34	FCC, HCP	240	6	NVT	2000	0.06
7	FCC, HCP, DIA, SC	1200	6	NVT	100	0.01	35	FCC, HCP	600	6	NVT	2000	0.02
8	FCC, HCP, DIA, SC	240	2	NVT	300	0.13	36	FCC(surf.)	792	0.2	NVT	300	0.69
9	FCC, HCP, DIA, SC	480	6	NVT	300	0.03	37	FCC(surf.)	792	2	NVT	300	0.00
10	FCC, HCP, DIA, SC	480	6	NVT	300	0.01	38	FCC(surf.)	792	6	NVT	300	0.00
11	FCC, HCP, DIA, SC	1200	6	NVT	300	0.01	39	FCC(surf.)	792	0.2	NVT	900	0.00
12	FCC, HCP	120	2	NVT	600	0.33	40	FCC(surf.)	792	2	NVT	900	0.05
13	FCC, HCP	240	6	NVT	600	0.06	41	FCC(surf.)	792	6	NVT	900	0.02
14	FCC, HCP	240	6	NVT	600	0.00	42	FCC(surf.)	792	0.2	NVT	1500	0.10
15	FCC, HCP	600	6	NVT	600	0.00	43	FCC(surf.)	792	2	NVT	1500	0.07
16	FCC, HCP	120	2	NVT	900	0.00	44	FCC(surf.)	792	6	NVT	1500	0.03
17	FCC, HCP	240	6	NVT	900	0.03	45	HCP(surf.)	792	0.2	NVT	300	0.10
18	FCC, HCP	240	6	NVT	900	0.05	46	HCP(surf.)	792	2	NVT	300	0.01
19	FCC, HCP	600	6	NVT	900	0.02	47	HCP(surf.)	792	6	NVT	300	0.00
20	FCC, HCP	120	2	NPT	900	0.00	48	HCP(surf.)	792	0.2	NVT	900	0.00
21	FCC, HCP	240	6	NPT	900	0.00	49	HCP(surf.)	792	2	NVT	900	0.01
22	FCC, HCP	240	6	NPT	900	0.00	50	HCP(surf.)	792	6	NVT	900	0.03
23	FCC, HCP	600	6	NPT	900	0.00	51	HCP(surf.)	792	0.2	NVT	1500	0.55
24	FCC, HCP	120	2	NVT	1200	0.00	52	HCP(surf.)	792	2	NVT	1500	0.04
25	FCC, HCP	240	6	NVT	1200	0.04	53	HCP(surf.)	792	6	NVT	1500	0.03
26	FCC, HCP	240	6	NVT	1200	0.05							
27	FCC, HCP	600	6	NVT	1200	0.02							

TABLE S3: Exploration strategy for the Al-Mg alloy system. For each iteration, we report the crystalline structure from which the initial structures are derived, the number of DPMD simulations, the length of DPMD trajectories, the statistical ensemble, the temperature of DPMD simulations and the portion of explored data sent to labeling. The pressure is 1 bar for the NPT ensembles.

Iter.	Crystal	#DPMD	Length [ps]	Ensemb.	T [K]	Labd. [%]	Iter.	Crystal	#DPMD	Length [ps]	Ensemb.	T [K]	Labd. [%]
0	FCC, HCP, DIA, SC	408	0.2	NVT	50	8.15	30	FCC, HCP	552	6	NVT	1500	0.14
1	FCC, HCP, DIA, SC	816	2	NVT	50	1.68	31	FCC, HCP	1104	6	NVT	1500	0.20
2	FCC, HCP, DIA, SC	816	6	NVT	50	0.43	32	FCC, HCP	276	2	NVT	2000	0.00
3	FCC, HCP, DIA, SC	1632	6	NVT	50	0.17	33	FCC, HCP	552	6	NVT	2000	0.33
4	FCC, HCP, DIA, SC	408	0.2	NVT	100	3.24	34	FCC, HCP	552	6	NVT	2000	0.31
5	FCC, HCP, DIA, SC	816	2	NVT	100	0.41	35	FCC, HCP	1104	6	NVT	2000	0.17
6	FCC, HCP, DIA, SC	816	6	NVT	100	0.12	36	FCC(surf.)	11,616	0.2	NVT	300	0.69
7	FCC, HCP, DIA, SC	1632	6	NVT	100	0.07	37	FCC(surf.)	11,616	2	NVT	300	0.07
8	FCC, HCP, DIA, SC	408	0.2	NVT	300	1.36	38	FCC(surf.)	11,616	6	NVT	300	0.00
9	FCC, HCP, DIA, SC	816	2	NVT	300	0.82	39	FCC(surf.)	11,616	6	NVT	300	0.01
10	FCC, HCP, DIA, SC	816	6	NVT	300	0.17	40	FCC(surf.)	11,616	0.2	NVT	900	0.13
11	FCC, HCP, DIA, SC	1632	6	NVT	300	0.05	41	FCC(surf.)	11,616	2	NVT	900	0.01
12	FCC, HCP	276	2	NVT	600	0.29	42	FCC(surf.)	11,616	6	NVT	900	0.02
13	FCC, HCP	552	6	NVT	600	0.26	43	FCC(surf.)	11,616	6	NVT	900	0.00
14	FCC, HCP	552	6	NVT	600	0.35	44	FCC(surf.)	11,616	0.2	NVT	1500	0.01
15	FCC, HCP	1104	6	NVT	600	0.03	45	FCC(surf.)	11,616	2	NVT	1500	0.01
16	FCC, HCP	276	2	NVT	900	0.52	46	FCC(surf.)	11,616	6	NVT	1500	0.02
17	FCC, HCP	552	6	NVT	900	0.50	47	FCC(surf.)	11,616	6	NVT	1500	0.03
18	FCC, HCP	552	6	NVT	900	0.08	48	HCP(surf.)	11,616	0.2	NVT	300	0.00
19	FCC, HCP	1104	6	NVT	900	0.00	49	HCP(surf.)	11,616	2	NVT	300	0.00
20	FCC, HCP	276	2	NPT	900	0.00	50	HCP(surf.)	11,616	6	NVT	300	0.00
21	FCC, HCP	552	6	NPT	900	0.00	51	HCP(surf.)	11,616	6	NVT	300	0.00
22	FCC, HCP	552	6	NPT	900	0.01	52	HCP(surf.)	11,616	0.2	NVT	900	0.00
23	FCC, HCP	1104	6	NPT	900	0.00	53	HCP(surf.)	11,616	2	NVT	900	0.00
24	FCC, HCP	276	2	NVT	1200	0.04	54	HCP(surf.)	11,616	6	NVT	900	0.00
25	FCC, HCP	552	6	NVT	1200	0.47	55	HCP(surf.)	11,616	6	NVT	900	0.00
26	FCC, HCP	552	6	NVT	1200	0.03	56	HCP(surf.)	11,616	0.2	NVT	1500	0.00
27	FCC, HCP	1104	6	NVT	1200	0.21	57	HCP(surf.)	11,616	2	NVT	1500	0.00
28	FCC, HCP	276	2	NVT	1500	0.00	58	HCP(surf.)	11,616	6	NVT	1500	0.01
29	FCC, HCP	552	6	NVT	1500	0.35	59	HCP(surf.)	11,616	6	NVT	1500	0.02

TABLE S4: Number of explored and labeled data by the DP-GEN scheme for pure Al, pure Mg, and Mg-Al alloy systems.

Systems		Al		Mg		Al-Mg alloys		
Type	Crystal	#atom	#Explored	#Labeled	#Explored	#Labeled	#Explored	#Labeled
Bulk	FCC	32	15,174,000	1,326	15,174,000	860	39,266,460	7,313
	HCP	16	15,174,000	908	15,174,000	760	18,999,900	2,461
	Diamond	16	5,058,000	1,026	5,058,000	543	5,451,300	2,607
	SC	8	5,058,000	713	5,058,000	234	2,543,940	667
Surface	FCC (100)	12	3,270,960	728	3,270,960	251	62,203,680	1,131
	FCC (110)	16 ^a ,20 ^b	3,270,960	838	3,270,960	353	10,744,2720	2,435
	FCC (111)	12	3,270,960	544	3,270,960	230	62,203,680	1,160
	HCP (0001)	12	3,270,960	39	3,270,960	109	62,203,680	176
	HCP (10 $\bar{1}$ 0)	12	3,270,960	74	3,270,960	167	62,203,680	203
	HCP (11 $\bar{2}$ 0)	16 ^a ,20 ^b	3,270,960	293	3,270,960	182	107,442,720	501
sum			60,089,760	6,489	60,089,760	3,689	529,961,760	18,654

^aPure Al

^bMg and Al-Mg alloy

TABLE S5: The size of supercells used for generating the vacancy and interstitial structures.

Mat.Proj.ID	# copies	N	Mat.Proj.ID	# copies	N	Mat.Proj.ID	# copies	N
mp-1016233	$2 \times 3 \times 2$	48	mp-1039141	$3 \times 3 \times 3$	54	mp-1094700	$1 \times 1 \times 1$	58
mp-1016271	$2 \times 2 \times 2$	64	mp-1039180	$1 \times 1 \times 1$	16	mp-1094961	$2 \times 2 \times 1$	32
mp-1023506	$2 \times 2 \times 1$	64	mp-1039192	$2 \times 2 \times 2$	48	mp-1094970	$2 \times 2 \times 2$	64
mp-1038779	$3 \times 3 \times 1$	54	mp-1094116	$1 \times 1 \times 1$	12	mp-1094987	$2 \times 2 \times 2$	32
mp-1038818	$2 \times 2 \times 2$	64	mp-1094664	$2 \times 2 \times 2$	32	mp-12766	$1 \times 1 \times 1$	27
mp-1038916	$2 \times 2 \times 1$	32	mp-1094666	$1 \times 1 \times 1$	16	mp-17659	$1 \times 1 \times 1$	53
mp-1038934	$3 \times 3 \times 3$	54	mp-1094683	$1 \times 1 \times 1$	58	mp-2151	$1 \times 1 \times 1$	29
mp-1039010	$2 \times 2 \times 2$	64	mp-1094685	$1 \times 1 \times 1$	58	mp-568106	$1 \times 1 \times 1$	108
mp-1039019	$3 \times 3 \times 3$	54	mp-1094692	$1 \times 1 \times 1$	87	mp-978271	$2 \times 2 \times 2$	32
mp-1039119	$2 \times 2 \times 2$	64						

TABLE S6: Surface formation energies of FCC Al.

Miller indices	DFT[58] [J/m ²]	DP [J/m ²]	MEAM [J/m ²]
(100)	0.92	0.95	1.09
(110)	0.98	0.99	1.14
(111)	0.80	0.82	0.75
(210)	1.02	1.03	1.21
(211)	0.98	0.99	1.02
(221)	0.95	0.93	0.82
(310)	0.99	1.03	1.20
(311)	0.98	0.97	1.10
(320)	1.01	1.03	1.18
(321)	0.96	0.98	1.07
(322)	0.90	0.91	0.86
(331)	0.96	0.96	1.03
(332)	0.91	0.89	0.80

TABLE S7: Surface formation energies of HCP Mg.

Miller indices	DFT[58] [J/m ²]	DP [J/m ²]	MEAM [J/m ²]
(0001)	0.54	0.58	0.71
(10 $\bar{1}$ 0)	0.60	0.62	0.72
(10 $\bar{1}$ 1)	0.63	0.66	0.76
(10 $\bar{1}$ 2)	0.70	0.73	0.80
(11 $\bar{2}$ 0)	0.72	0.73	0.76
(11 $\bar{2}$ 1)	0.76	0.75	0.78
(20 $\bar{2}$ 1)	0.77	0.77	0.83
(2 $\bar{1}$ $\bar{1}$ 2)	0.74	0.73	0.77
(21 $\bar{3}$ 0)	0.70	0.72	0.76
(21 $\bar{3}$ 1)	0.73	0.74	0.78
(21 $\bar{3}$ 2)	0.74	0.74	0.80
(22 $\bar{4}$ 1)	0.75	0.75	0.78

TABLE S8: Equilibrium properties of Mg.

Mg	Exp.	DFT	DP	MEAM
E_0 [eV/atom]	-1.51 ^a	-1.489	-1.487	-1.510
V_0 [\AA^3 /atom]	23.24 ^b	22.89	22.83	23.04
E_{vf} [eV]	0.79 ^c	0.79	0.67	0.87
		2.16	2.17	1.76
		2.18	2.14	1.76
E_{if} [eV]	-	2.19	2.23	1.56
		2.16	2.14	1.56
C_{11} [GPa]	63.5 ^d	61.0	59.9	59.7
C_{33} [GPa]	66.5 ^d	64.5	71.3	60.7
C_{12} [GPa]	25.9 ^d	28.2	26.1	23.2
C_{13} [GPa]	21.7 ^d	20.7	19.2	23.6
C_{44} [GPa]	18.4 ^d	16.0	16.7	16.7
C_{66} [GPa]	18.8 ^d	18.4	16.8	18.2
B_V [GPa]	36.9 ^d	36.3	35.6	35.7
G_V [GPa]	19.4 ^d	17.9	18.6	17.6
γ_{sf} [J/m ²]	0.078 ^e	0.0339 ^f	0.0384	0.0218
γ_{tsf} [J/m ²]	-	0.0414 ^f	0.0388	0.0219
T_m [K]	922	-	870	765
ΔH_f [kJ/mol]	9.0(± 0.2) ^l	-	8.7	9.1

^aReference [62]^bReference [63], 300K^cReference [64]^dReference [65]^eReference [66]^fReference [67]

TABLE S9: The formation energy and volume per atom of Mg-Al alloys, displayed in ascending order of Mg concentration and descending order of structure stability. The numbers in the parentheses give the difference between the DP/MEAM method and the DFT calculation.

Mat.Proj.ID	N	c_{Mg}	$E_{\text{af}}^{\text{DFT}}$ [eV/atom]	$E_{\text{af}}^{\text{DP}}$ [eV/atom]	$E_{\text{af}}^{\text{MEAM}}$ [eV/atom]	V_0^{DFT} [\AA^3]	V_0^{DP} [\AA^3]	V_0^{MEAM} [\AA^3]
mp-1038916	8	25.0%	0.005	0.007 (2)	0.091 (86)	17.79	17.78 (0.1%)	19.25 (8.2%)
mp-1039119	8	25.0%	0.020	0.021 (1)	-0.013 (33)	17.82	17.89 (0.4%)	19.29 (8.3%)
mp-1039180	16	25.0%	0.094	0.090 (4)	0.206 (112)	18.09	18.09 (0.0%)	18.32 (1.3%)
mp-1094116	12	33.3%	-0.013	-0.007 (6)	0.101 (114)	18.79	18.91 (0.6%)	20.31 (8.1%)
mp-1039192	6	33.3%	0.662	0.705 (43)	0.595 (67)	26.43	26.84 (1.6%)	28.58 (8.1%)
mp-568106	108	38.0%	0.023	0.021 (2)	0.016 (7)	18.72	18.66 (0.3%)	20.26 (8.2%)
mp-17659	53	43.4%	-0.019	-0.014 (5)	0.129 (149)	19.27	19.34 (0.4%)	20.76 (7.7%)
mp-12766	27	48.1%	0.061	0.061 (0)	0.237 (175)	19.54	19.51 (0.2%)	20.43 (4.6%)
mp-1039141	2	50.0%	-0.003	-0.003 (0)	-0.094 (91)	19.22	19.22 (0.0%)	20.71 (7.8%)
mp-1094987	4	50.0%	0.010	0.010 (0)	-0.128 (138)	19.22	19.30 (0.4%)	20.50 (6.7%)
mp-1038779	6	50.0%	0.030	0.033 (3)	0.153 (124)	19.49	19.43 (0.3%)	21.27 (9.1%)
mp-1039019	2	50.0%	0.043	0.045 (2)	0.158 (115)	19.41	19.39 (0.1%)	21.20 (9.2%)
mp-1038934	2	50.0%	0.062	0.063 (1)	-0.032 (93)	19.41	19.55 (0.7%)	20.29 (4.5%)
mp-1039010	8	50.0%	0.439	0.433 (5)	0.230 (209)	23.71	23.87 (0.7%)	23.64 (0.3%)
mp-1038818	8	50.0%	0.885	0.890 (5)	0.768 (118)	33.34	33.74 (1.2%)	31.88 (4.4%)
mp-1094664	4	50.0%	0.592	0.593 (0)	0.451 (141)	29.15	28.73 (1.4%)	29.60 (1.6%)
mp-1094685	58	55.2%	-0.019	-0.007 (13)	0.071 (90)	19.88	19.88 (0.0%)	21.33 (7.3%)
mp-1094692	87	55.2%	-0.015	-0.003 (12)	0.065 (81)	19.94	19.95 (0.0%)	21.33 (7.0%)
mp-1094683	58	55.2%	-0.009	0.005 (14)	0.076 (85)	19.98	19.97 (0.0%)	21.54 (7.8%)
mp-2151	29	58.6%	-0.025	-0.010 (15)	0.049 (74)	20.07	20.09 (0.1%)	21.28 (6.0%)
mp-1094700	58	62.1%	-0.018	-0.003 (15)	0.029 (47)	20.32	20.33 (0.1%)	21.50 (5.8%)
mp-1094970	8	75.0%	0.004	0.001 (3)	-0.101 (104)	20.90	20.87 (0.2%)	21.81 (4.3%)
mp-978271	4	75.0%	0.005	0.003 (2)	-0.046 (50)	20.95	20.96 (0.1%)	21.99 (5.0%)
mp-1094961	8	75.0%	0.012	0.009 (2)	-0.072 (84)	21.01	21.04 (0.2%)	21.67 (3.1%)
mp-1016233	4	75.0%	0.021	0.021 (0)	0.031 (9)	20.98	21.01 (0.1%)	22.20 (5.8%)
mp-1094666	16	75.0%	0.043	0.042 (1)	-0.079 (122)	20.85	20.80 (0.2%)	21.36 (2.5%)
mp-1016271	8	87.5%	0.011	0.010 (1)	-0.021 (32)	21.88	21.86 (0.1%)	22.51 (2.9%)
mp-1023506	16	93.8%	0.006	0.005 (0)	-0.010 (15)	22.36	22.32 (0.2%)	22.82 (2.1%)

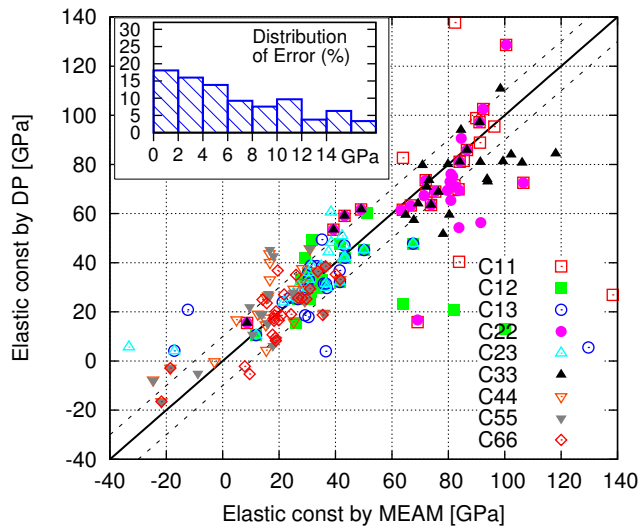


FIG. S3: Elastic constants computed by MEAM compared with those computed by DFT.

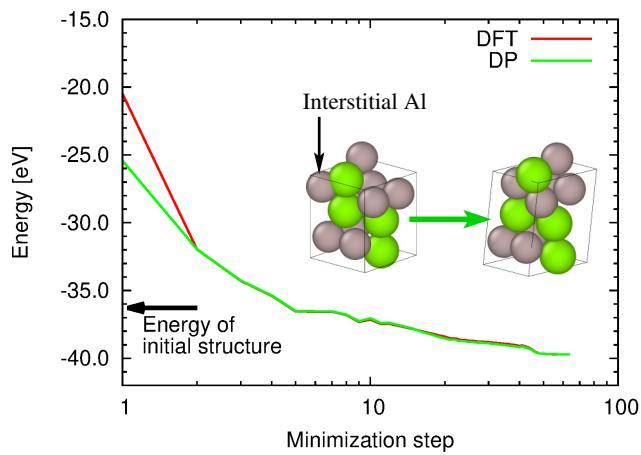


FIG. S4: Comparison of energies predicted by DFT and DP along the Al interstitial relaxation pathway within DFT. The interstitial structure is generated from mp-1094116. The insert shows the initial and relaxed interstitial configurations.

* Electronic address: wang_han@iapcm.ac.cn

† Electronic address: weinan@math.princeton.edu

- [1] John Edward Jones. On the determination of molecular fields. In *Proceedings of the Royal Society of London A: Mathematical, Physical and Engineering Sciences*, volume 106, pages 463–477. The Royal Society, 1924.
- [2] Frank H Stillinger and Thomas A Weber. Computer simulation of local order in condensed phases of silicon. *Physical Review B*, 31(8):5262, 1985.
- [3] Murray S Daw and Michael I Baskes. Embedded-atom method: Derivation and application to impurities, surfaces, and other defects in metals. *Physical Review B*, 29(12):6443, 1984.
- [4] Alex D MacKerell Jr, Donald Bashford, MLDR Bellott, Roland Leslie Dunbrack Jr, Jeffrey D Evanseck, Martin J Field, Stefan Fischer, Jiali Gao, H Guo, Sookhee Ha, et al. All-atom empirical potential for molecular modeling and dynamics studies of proteins. *The Journal of Physical Chemistry B*, 102(18):3586–3616, 1998.
- [5] Junmei Wang, Piotr Cieplak, and Peter A Kollman. How well does a restrained electrostatic potential (resp) model perform in calculating conformational energies of organic and biological molecules? *Journal of Computational Chemistry*, 21(12):1049–1074, 2000.
- [6] Adri CT Van Duin, Siddharth Dasgupta, Francois Lorient, and William A Goddard. Reaxff: a reactive force field for hydrocarbons. *The Journal of Physical Chemistry A*, 105(41):9396–9409, 2001.
- [7] Jörg Behler and Michele Parrinello. Generalized neural-network representation of high-dimensional potential-energy surfaces. *Physical Review Letters*, 98(14):146401, 2007.
- [8] Albert P Bartók, Mike C Payne, Risi Kondor, and Gábor Csányi. Gaussian approximation potentials: The accuracy of quantum mechanics, without the electrons. *Physical Review Letters*, 104(13):136403, 2010.
- [9] Matthias Rupp, Alexandre Tkatchenko, Klaus-Robert Müller, and O Anatole VonLilienfeld. Fast and accurate modeling of molecular atomization energies with machine learning. *Physical Review Letters*, 108(5):058301, 2012.
- [10] Grégoire Montavon, Matthias Rupp, Vivekanand Gobre, Alvaro Vazquez-Mayagoitia, Katja Hansen, Alexandre Tkatchenko, Klaus-Robert Müller, and O Anatole Von Lilienfeld. Machine learning of molecular electronic properties in chemical compound space. *New Journal of Physics*, 15(9):095003, 2013.
- [11] Venkatesh Botu, Rohit Batra, James Chapman, and Rampi Ramprasad. Machine learning force fields: construction, validation, and outlook. *The Journal of Physical Chemistry C*, 121(1):511–522, 2016.
- [12] Stefan Chmiela, Alexandre Tkatchenko, Huziel E Sauceda, Igor Poltavsky, Kristof T Schütt, and Klaus-Robert Müller. Machine learning of accurate energy-conserving molecular force fields. *Science Advances*, 3(5):e1603015, 2017.
- [13] Kristof Schütt, Pieter-Jan Kindermans, Huziel Enoc Sauceda Felix, Stefan Chmiela, Alexandre Tkatchenko, and Klaus-Robert Müller. Schnet: A continuous-filter convolutional neural network for modeling quantum interactions. In *Advances in Neural Information Processing Systems*, pages 992–1002, 2017.
- [14] Albert P Bartók, Sandip De, Carl Poelking, Noam Bernstein, James R Kermode, Gábor Csányi, and Michele Cerrioni. Machine learning unifies the modeling of materials and molecules. *Science advances*, 3(12):e1701816, 2017.
- [15] Justin S Smith, Olexandr Isayev, and Adrian E Roitberg. ANI-1: an extensible neural network potential with dft accuracy at force field computational cost. *Chemical Science*, 8(4):3192–3203, 2017.
- [16] Jiequn Han, Linfeng Zhang, Roberto Car, and Weinan E. Deep Potential: a general representation of a many-body potential energy surface. *Communications in Computational Physics*, 23(3):629–639, 2018.
- [17] Xin Chen, Mathias Siggaard Jørgensen, Jun Li, and Bjørk Hammer. Atomic energies from a convolutional neural network. *Journal of chemical theory and computation*, 14:3933–3942, 2018.
- [18] Linfeng Zhang, Jiequn Han, Han Wang, Roberto Car, and Weinan E. Deep potential molecular dynamics: A scalable model with the accuracy of quantum mechanics. *Physical review letters*, 120:143001, Apr 2018.
- [19] Linfeng Zhang, Jiequn Han, Han Wang, Wissam A Saidi, Roberto Car, and Weinan E. End-to-end symmetry preserving inter-atomic potential energy model for finite and extended systems. *arXiv preprint arXiv:1805.09003*, 2018.
- [20] Burr Settles. Active learning. *Synthesis Lectures on Artificial Intelligence and Machine Learning*, 6(1):1–114, 2012.
- [21] Neil Rubens, Mehdi Elahi, Masashi Sugiyama, and Dain Kaplan. Active learning in recommender systems. In *Recommender systems handbook*, pages 809–846. Springer, 2015.
- [22] John P Perdew, Kieron Burke, and Matthias Ernzerhof. Generalized gradient approximation made simple. *Physical review letters*, 77(18):3865, 1996.
- [23] Georg Kresse and Jürgen Furthmüller. Efficient iterative schemes for ab initio total-energy calculations using a plane-wave basis set. *Physical review B*, 54(16):11169, 1996.
- [24] Georg Kresse and Jürgen Furthmüller. Efficiency of ab-initio total energy calculations for metals and semiconductors using a plane-wave basis set. *Computational materials science*, 6(1):15–50, 1996.
- [25] Hendrik J Monkhorst and James D Pack. Special points for brillouin-zone integrations. *Physical review B*, 13(12):5188, 1976.
- [26] Anubhav Jain, Shyue Ping Ong, Geoffroy Hautier, Wei Chen, William Davidson Richards, Stephen Dacek, Shreyas Cholia, Dan Gunter, David Skinner, Gerbrand Ceder, et al. The materials project: A materials genome approach to accelerating materials innovation. *Apl Materials*, 1(1):011002, 2013.
- [27] Shyue Ping Ong, William Davidson Richards, Anubhav Jain, Geoffroy Hautier, Michael Kocher, Shreyas Cholia, Dan Gunter, Vincent L Chevrier, Kristin A Persson, and Gerbrand Ceder. Python materials genomics (pymatgen): A robust, open-source python library for materials analysis. *Computational Materials Science*, 68:314–319, 2013.
- [28] Evgeny V Podryabinkin and Alexander V Shapeev. Active learning of linearly parametrized interatomic potentials. *Computational Materials Science*, 140:171–180, 2017.
- [29] Justin S Smith, Ben Nebgen, Nicholas Lubbers, Olexandr

- Isayev, and Adrian E Roitberg. Less is more: Sampling chemical space with active learning. *The Journal of Chemical Physics*, 148(24):241733, 2018.
- [30] John E Herr, Kun Yao, Ryker McIntyre, David W Toth, and John Parkhill. Metadynamics for training neural network model chemistries: A competitive assessment. *The Journal of Chemical Physics*, 148(24):241710, 2018.
- [31] Luigi Bonati and Michele Parrinello. Silicon liquid structure and crystal nucleation from ab-initio deep metadynamics. *arXiv preprint arXiv:1809.11088*, 2018.
- [32] Justin S Smith, Olexandr Isayev, and Adrian E Roitberg. ANI-1, a data set of 20 million calculated off-equilibrium conformations for organic molecules. *Scientific data*, 4:170193, 2017.
- [33] Albert P Bartok, James Kermode, Noam Bernstein, and Gabor Csanyi. Machine learning a general purpose interatomic potential for silicon. *arXiv preprint arXiv:1805.01568*, 2018.
- [34] Linfeng Zhang, Han Wang, and Weinan E. Reinforced dynamics for enhanced sampling in large atomic and molecular systems. *The Journal of chemical physics*, 148(12):124113, 2018.
- [35] Weinan E. *Principles of multiscale modeling*. Cambridge University Press, 2011.
- [36] Diederik Kingma and Jimmy Ba. Adam: a method for stochastic optimization. In *Proceedings of the International Conference on Learning Representations (ICLR)*, may 2015.
- [37] MI Baskes. Modified embedded-atom potentials for cubic materials and impurities. *Physical review B*, 46(5):2727, 1992.
- [38] Bohumir Jelinek, Sebastien Groh, Mark F Horstemeyer, Jeffery Houze, Seong-Gon Kim, Gregory J Wagner, Amitava Moitra, and Michael I Baskes. Modified embedded atom method potential for al, si, mg, cu, and fe alloys. *Physical Review B*, 85(24):245102, 2012.
- [39] Han Wang, Linfeng Zhang, Jiequn Han, and Weinan E. DeePMD-kit: A deep learning package for many-body potential energy representation and molecular dynamics. *Computer Physics Communications*, 228:178 – 184, 2018.
- [40] Steve Plimpton. Fast parallel algorithms for short-range molecular dynamics. *Journal of computational physics*, 117(1):1–19, 1995.
- [41] Cox J. D., Wagman D. D., and Medvedev V. A. *CO-DATA Key Values for Thermodynamics*. Hemisphere Publishing Corp., 1989.
- [42] Ann S Cooper. Precise lattice constants of germanium, aluminum, gallium arsenide, uranium, sulphur, quartz and sapphire. *Acta Crystallographica*, 15(6):578–582, 1962.
- [43] W Triftshäuser. Positron trapping in solid and liquid metals. *Physical Review B*, 12(11):4634, 1975.
- [44] MJ Fluss, L C. Smedskjaer, MK Chason, DG Legnini, and RW Siegel. Measurements of the vacancy formation enthalpy in aluminum using positron annihilation spectroscopy. *Physical Review B*, 17(9):3444, 1978.
- [45] Randolph Q Hood, PRC Kent, and Fernando A Reberedo. Diffusion quantum monte carlo study of the equation of state and point defects in aluminum. *Physical Review B*, 85(13):134109, 2012.
- [46] GN Kamm and GA Alers. Low-temperature elastic moduli of aluminum. *Journal of Applied Physics*, 35(2):327–330, 1964.
- [47] VC Kannan and G Thomas. Dislocation climb and de-termination of stacking-fault energies in al and al-1% mg. *Journal of Applied Physics*, 37(6):2363–2370, 1966.
- [48] PS Dobson, PJ Goodhew, and RE Smallman. Climb kinetics of dislocation loops in aluminium. *Philosophical Magazine*, 16(139):9–22, 1967.
- [49] Jean-Pierre Tartour and Jack Washburn. Climb kinetics of dislocation loops in aluminium. *Philosophical Magazine*, 18(156):1257–1267, 1968.
- [50] Michael J Mills and Pierre Stadelmann. A study of the structure of lomer and 60 dislocations in aluminium using high-resolution transmission electron microscopy. *Philosophical Magazine A*, 60(3):355–384, 1989.
- [51] Dongdong Zhao, Ole Martin Løvvik, Knut Marthinsen, and Yanjun Li. Impurity effect of mg on the generalized planar fault energy of al. *Journal of materials science*, 51(14):6552–6568, 2016.
- [52] Marvin Ross, Lin H Yang, and Reinhard Boehler. Melting of aluminum, molybdenum, and the light actinides. *Physical Review B*, 70(18):184112, 2004.
- [53] J Bouchet, F Bottin, G Jomard, and G Zérah. Melting curve of aluminum up to 300 gpa obtained through ab initio molecular dynamics simulations. *Physical Review B*, 80(9):094102, 2009.
- [54] Richard Addison McDonald. Enthalpy, heat capacity, and heat of fusion of aluminum from 366. degree. to 1647. degree. k. *Journal of Chemical and Engineering Data*, 12(1):115–118, 1967.
- [55] Andreas Meyer. The measurement of self-diffusion coefficients in liquid metals with quasielastic neutron scattering. In *EPJ Web of Conferences*, volume 83, page 01002. EDP Sciences, 2015.
- [56] R t Stedman and G Nilsson. Dispersion relations for phonons in aluminum at 80 and 300 k. *Physical Review*, 145(2):492, 1966.
- [57] Yoshio Waseda. The structure of non-crystalline materials. *Liquids and Amorphous Solids*, 1980.
- [58] Richard Tran, Zihan Xu, Balachandran Radhakrishnan, Donald Winston, Wenhao Sun, Kristin A Persson, and Shyue Ping Ong. Surface energies of elemental crystals. *Scientific data*, 3:160080, 2016.
- [59] Mariette Hellenbrandt. The inorganic crystal structure database (icsd) present and future. *Crystallography Reviews*, 10(1):17–22, 2004.
- [60] Samad Hajinazar, Junping Shao, and Aleksey N Kolmogorov. Stratified construction of neural network based interatomic models for multicomponent materials. *Physical Review B*, 95(1):014114, 2017.
- [61] Kaiming He, Xiangyu Zhang, Shaoqing Ren, and Jian Sun. Deep residual learning for image recognition. In *Proceedings of the IEEE conference on computer vision and pattern recognition*, pages 770–778, 2016.
- [62] Charles Kittel. *Introduction to solid state physics*. Wiley New York, 2004.
- [63] FW Von Batchelder and RF Raeuchle. Lattice constants and brillouin zone overlap in dilute magnesium alloys. *Physical Review*, 105(1):59, 1957.
- [64] P Tzanetakis, J Hillairet, and G Revel. The formation energy of vacancies in aluminium and magnesium. *physica status solidi (b)*, 75(2):433–439, 1976.
- [65] Leon J Slutsky and CW Garland. Elastic constants of magnesium from 4.2 k to 300 k. *Physical Review*, 107(4):972, 1957.
- [66] DH Sastry, YVRK Prasad, and KI Vasu. On the stacking fault energies of some close-packed hexagonal metals.

Scripta Metallurgica, 3(12):927–929, 1969.

- [67] SH Zhang, IJ Beyerlein, Dominik Legut, ZH Fu, Z Zhang, SL Shang, ZK Liu, TC Germann, and RF Zhang. First-principles investigation of strain effects on the stacking fault energies, dislocation core structure, and peierls stress of magnesium and its alloys. *Physical Review B*, 95(22):224106, 2017.
- [68] These structures are mp-1038916, mp-1094116, mp-568106, mp-17659, mp-12766, mp-1039141, mp-1094685, mp-2151, mp-1094700, mp-1094970, mp-1016271, mp-1023506